PNAS RESEARCH ARTICLE | NEUROSCIENCE ENVIRONMENTAL SCIENCES

Wide bandgap semiconductor nanomembranes as a long-term biointerface for flexible, implanted neuromodulator

Tuan-Khoa Nguyen[a], Matthew Barton[b], Aditya Ashok[a,c], Thanh-An Truong[a], Sharda Yadav[a], Michael Leitch[b], Thanh-Vinh Nguyen[d], Navid Kashaninejad[a], Toan Dinh[e], Leonie Hold[a], Yusuke Yamauchi[c,f,g], Nam-Trung Nguyen[a], and Hoang-Phuong Phan[a,h,1]

Edited by Philipp Gutruf, The University of Arizona; received February 23, 2022; accepted July 7, 2022 by Editorial Board Member Yonggang Huang

Electrical neuron stimulation holds promise for treating chronic neurological disorders, including spinal cord injury, epilepsy, and Parkinson's disease. The implementation of ultrathin, flexible electrodes that can offer noninvasive attachment to soft neural tissues is a breakthrough for timely, continuous, programable, and spatial stimulations. With strict flexibility requirements in neural implanted stimulations, the use of conventional thick and bulky packages is no longer applicable, posing major technical issues such as short device lifetime and long-term stability. We introduce herein a concept of long-lived flexible neural electrodes using silicon carbide (SiC) nanomembranes as a faradic interface and thermal oxide thin films as an electrical barrier layer. The SiC nanomembranes were developed using a chemical vapor deposition (CVD) process at the wafer level, and thermal oxide was grown using a high-quality wet oxidation technique. The proposed material developments are highly scalable and compatible with MEMS technologies, facilitating the mass production of long-lived implanted bioelectrodes. Our experimental results showed excellent stability of the SiC/silicon dioxide (SiO_2) bioelectronic system that can potentially last for several decades with well-maintained electronic properties in biofluid environments. We demonstrated the capability of the proposed material system for peripheral nerve stimulation in an animal model, showing muscle contraction responses comparable to those of a standard non-implanted nerve stimulation device. The design concept, scalable fabrication approach, and multimodal functionalities of SiC/SiO_2 flexible electronics offer an exciting possibility for fundamental neuroscience studies, as well as for neural stimulation–based therapies.

flexible electronics | implanted applications | neuron modulators | bioencapsulation | long-term stability

Significance

Implanted electronics are promising tools for cellular activity monitoring and neural stimulation for treating neurological disorders and restoring body functions. However, since these systems typically require direct interfaces with biofluids, maintaining their long-term operation as implantable devices is a daunting challenge. This work introduces a wide bandgap material system offering desirable attributes in this context. The implantable bioelectronic system consists of crystalline silicon carbide (SiC) nanomembranes as a faradic interface and silicon dioxide (SiO_2) as an encapsulation layer, showing notable electrical stability while maintaining its biointerfaces and biosensing functionality. We demonstrated multiple modalities of impedance/temperature sensors and implantable electrodes for peripheral neural stimulation. The SiC/SiO_2 flexible electronic system opens avenues for implanted bioelectronics in neuroscience and neural stimulation–based therapies.

Neurological disorders such as Parkinson's disease, traumatic brain injuries, and spinal cord injuries are the leading movement disorders with low probability of recovery (1, 2). Biomedical innovations that can enhance the restoration and regeneration of dysfunctions caused by neurological injuries have attracted a great deal of interest in improving the quality of life for patients and offering substantial economic benefits to society. Utilizing implanted neuromodulation devices is an advanced technology for the diagnosis and treatment of neurological disorders (3–6). For instance, deep brain stimulators are widely deployed for the treatment of Parkinson's disease, in which electrical stimuli produced from implanted electrodes can facilitate the regulation of dysfunctional brain regions (7, 8). A vagus nerve stimulation technique, which sends electrical impulses along nerve systems to the brainstem, was approved by the U.S. Food and Drug Administration for its proven efficacy in managing epilepsy in patients who do not adequately respond to antiseizure medications (9). Recent advances in neuromodulation through the electrical excitation of the peripheral nervous system provide promising paths for the restoration of motor neurons and the subsequent reactivation of muscle contraction. These capabilities further promote movement control of paralyzed limbs in patients with spinal cord injuries (10, 11).

Preclinical outcomes over the last decade have documented the remarkable development and innovation of advanced bioimplantable electronics for neuron stimulation (12–15). As such, there are two current mainstream neuromodulation systems: 1) intraneural electrodes, which can penetrate deeply into neural tissues, and 2) extraneural electrodes, which enable conformal contacts with the curvilinear surface of neural tissue. Intraneural devices, such as the Utah slanted electrode arrays, offer several advantages, such as close proximity to the target nerve and the capability to individually activate nerve fascicles (16). Nevertheless, extraneural approaches are preferred due to a lower risk of nerve damage and potentially higher resolution for spatial physiological mapping (17). Flexible electronics are considered the backbone technology for the realization of modern extraneural stimulators, in which the integration of soft

The authors declare no competing interest.

This article is a PNAS Direct Submission. P.G. is a guest editor invited by the Editorial Board.

[1]To whom correspondence may be addressed: Email: hp.phan@unsw.edu.au.

This article contains supporting information online at http://www.pnas.org/lookup/suppl/doi:10.1073/pnas.2203287119/-/DCSupplemental.

Published August 8, 2022.

semiconductors, ultrathin metallic interconnectors, and polymeric substrates offers ideal mechanical matching between functional devices and tissues (6, 13, 14, 18). Several types of distributed arrays of electrodes on soft substrates, combined with wireless communication modules (e.g., near-field communication), have shown potential for the monitoring and treatment of neural disorders (19, 20). Due to the minimized thickness requirement of constructing elements to facilitate mechanical flexibility, most existing material systems for soft electronics are bound for degradable devices with limited lifetimes due to hydrolysis degradations when implanted inside the human body (8, 21). However, for treatments of chronic diseases, long-lived flexible, implanted electronics that can last a patient's lifetime (e.g., several decades) are demanded (21, 22).

Extensive efforts have been dedicated to pushing the limit of durability and lifetime operation for implanted devices. For example, a soft neural interface (i.e., E-dura) that can match the mechanical behavior of the dura mater was demonstrated for a period of more than 6 wk (23). As such, the flexible, implanted platform, incorporating coated platinum (Pt)-silicone electrodes with gold interconnects on a flexible silicon (Si) substrate, provides electrochemical spinal neuromodulation that can restore locomotion for spinal cord injuries. Additionally, micro- and nanoscale metallic glasses were employed as implantable, robust, and multifunctional neuroprobes for the brain-machine interface for a longer in vivo treatment of up to 12 wk (24). A neural matrix for brain mapping was introduced to offer stable in vivo neural recordings in rodents and nonhuman primates. The device's life span was projected to be up to 6 y at a relatively low dissolution rate of silicon dioxide (SiO_2) (25). A fully covered biobarrier approach employed thermal oxide nanomembranes to facilitate a capacitive coupling interface for continuous cardiovascular electrophysiological mapping (26). Nevertheless, these platforms fail to offer direct electronics-tissue interfaces, limiting their potential for extracellular stimulations. One of the major challenges for the direct interface with biological tissue is that it would severely damage thin-film electrodes, especially with an applied electrical field for tissue stimulations. To overcome this, nanothin titanium disilicide films were introduced as a simultaneous faradic interface and biobarrier, bypassing the limitation in capacitive interfaces. However, this platform still inherited the limited electronic functionality of metal-based materials (27). The shortfall in the material library of robust biobarriers and functional biointerfaces for prolonged implantable electronics raises the demand for thin-film materials that can provide mechanical deformability and reliable operations in biofluids (28). In addition, there are limited reports for the long-lived implantable electronics that offer simultaneous nerve stimulation and multivariable biological sensing on living models or preclinical studies.

This paper presents a robust bioelectronic platform incorporating nanomembranes of the silicon carbide (SiC) biointerface and SiO_2 biobarrier for long-term bioimplanted applications. Our fabrication approach employs micro-electromechanical systems (MEMS)-compatible processes to form SiC/SiO_2 films using an epitaxial deposition of SiC and thermal oxidation for SiO_2. This is attributed to the chemical inertness of SiC material at elevated temperatures, allowing for in situ passivation with the thermal oxidation process. Experimental results demonstrate the excellent mechanical flexibility of the proposed electronic platform, along with long-term stability in biofluid environments. In vivo animal studies provide the proof of concept, using our material system for peripheral nerve excitation to facilitate muscle contraction. Our proposed platform documents promising possibilities toward long-term, multimodal, flexible bioelectronics for neuromodulation applications.

Results and Discussion

Concept of Implantable SiC Electronics for Nerve Stimulation. Fig. 1*A* shows the conceptual neuromodulation of long-lived bioimplanted SiC electronics to recover critical communication between the central nervous system and neuromuscular junctions. The system, via electronics-nerve interfaces, has potential as a long-term, therapeutic modality for movement restoration from chronic motor-based disorders, such as muscle/nerve stimulations for peripheral nerve regeneration and vagal modulations for treatments of heart conditions (e.g., hypertension and heart failure) (29), epileptic seizure (30), and depression (31). Desired features include well-matched mechanical flexibility with soft tissue, together with the capabilities of bioelectronic modality for neuron stimulation and real-time biophysical sensing (Fig. 1*B*). Fig. 1*C* illustrates the layered structure of long-lived implantable SiC bioelectronics, in which highly doped SiC provides a direct electronic interface (i.e., faradic interface) with tissue, while the SiO_2 membrane functions as a long-term stable biobarrier. In addition to their excellent tolerance to hydrolysis, both SiC and thermal oxide exhibit high dielectric constants (9.72 for SiC and 3.70 for SiO_2) and optical transparency (over 70% in 200-nm-thick SiC and nearly 100% in 600-nm-thick SiO_2 in the visible wavelengths), suggesting a

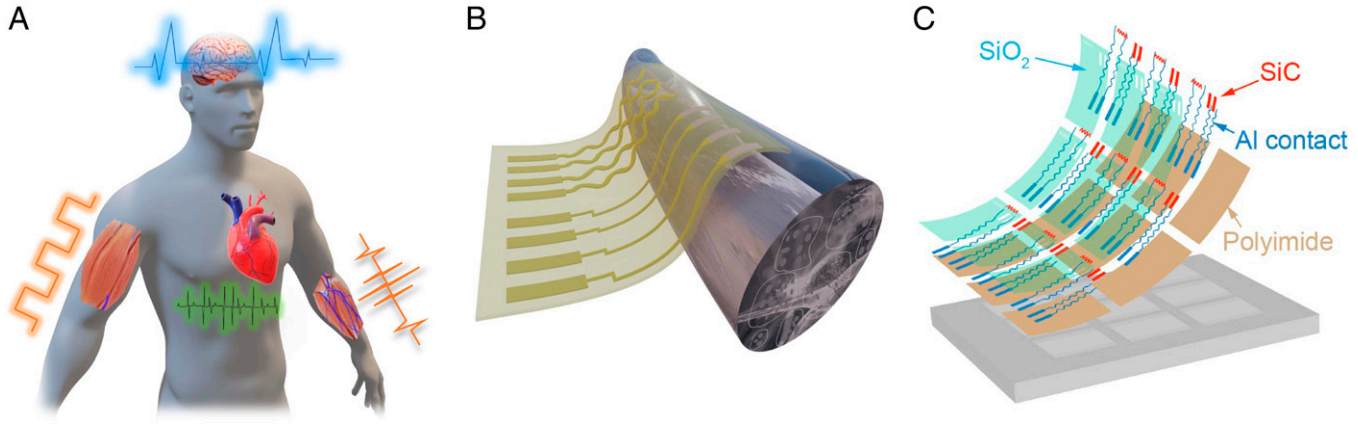

Fig. 1. Implanted SiC electronics for the nerve stimulation protocol. (*A*) Concept of SiC/SiO_2 electronics for neuromodulation, promoting the recovery of motor and physiological functions. (*B*) Schematic illustration of the flexible SiC/SiO_2 wrapped around a sciatic nerve for long-term electrical stimuli and sensing. (*C*) Exploded view of the proposed flexible SiC/SiO_2 bioelectronic system (Al: aluminum).

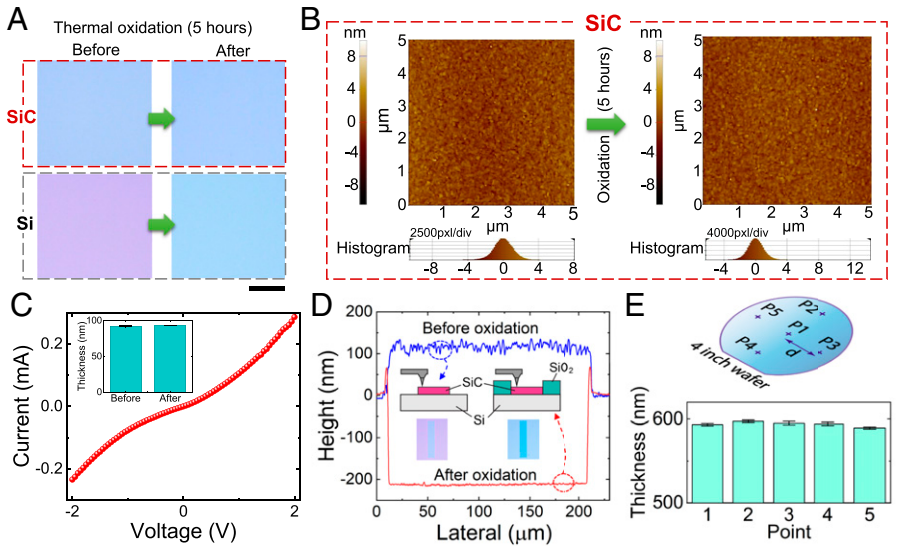

Fig. 2. Characterization of the SiC/SiO_2 platform fabricated with a CMOS-compatible thermal oxidation process. (*A*) Colorimetric observation under optical microscopy indicates no color change for SiC after the thermal oxidation for 5 h, while Si clearly changed from purple to light blue (scale bar, 100 µm). (*B*) Atomic force microscopy inspection of SiC surface morphology before and after the oxidation process. (*C*) I-V characteristics of SiC after oxidation. *Inset*: Thickness of SiC before and after oxidation. (*D*) Step height change after oxidation for SiC-patterned samples. (*E*) Uniformity of SiO_2 thickness across a 6-inch SiC-on-Si wafer after oxidation.

promising possibility for additional optoelectronic applications. Metal interconnects for the SiC electrodes were formed by conventional lithography processes (i.e., sputtering and wet etching; see *Methods*). A thin polyimide film with a thickness of approx. 10 µm was spin coated and utilized as the host substrate for the flexible device. Subsequently, the etching process of the initial Si carrier layer (380 µm thick), incorporating deep reactive ion etching and xenon difluoride etching, yields SiC/SiO_2 structures on the flexible substrate. Due to the extremely low bending stiffness in the ultrathin SiC and thermal oxide nanomembranes, along with the intrinsic mechanical flexibility of the polyimide film, our platform can offer conformal contact with neural tissue, primarily enabling the SiC electrodes to wrap around peripheral nerves for electrical stimulation. Electrical stimulation of peripheral nerves in an animal model is expected to evoke corresponding muscle activity, suggesting a promising pathway to regain limb control for patients with spinal cord injuries. A detailed description of the fabrication approach and material processing can be found in *Methods* and *SI Appendix*, Notes S1 and S2 and Fig. S2.

Formation of the SiC and SiO_2 Hybrid Structure. Nanothin SiC films were deposited on a Si substrate using a chemical vapor deposition (CVD) process inside a hot wall chamber at low pressure (32, 33). Details of the characterization of as-grown 3C-SiC nanomembranes can be found in our previous study, which showed the film as a single crystalline 3C-SiC on Si and was confirmed by selected area electron diffraction, with the crystallography orientation along the (100) direction measured by X-ray diffraction analysis (34). SiC electrodes were first patterned using standard photolithography and inductively coupled plasma (ICP) etching (see *Methods*). The exposed Si areas were selectively oxidized inside a controlled humidity chamber at 900 °C for a duration of 5 h (Fig. 2*A*). This is attributed to the excellent oxidation tolerance of SiC, as shown by a colorimetric observation under an optical microscope (Olympus MX50AF-IC), whereas Si reacted with vaporized water molecules ($Si + H_2O \rightarrow SiO_2 + 2H_2$) and turned from purple to light blue, as shown in Fig. 2*A*. The surface morphology and roughness of the SiC layer before and after oxidation were characterized by an atomic force microscope (i.e., Park Atomic force microscopes (AFM) NX20), showing no significant change (root mean square of approx. 2 nm). This indicates the stability of SiC at a high temperature of up to 900 °C in a wet oxidation condition (Fig. 2*B*). The thicknesses of the SiC film before and after oxidation were also quantified using a thin-film measurement (i.e., Nanometrics AFT 210), showing a consistent value of approx. 90 nm. By directly placing contact probes on the SiC surface after thermal oxidation without the requirement for hydrofluoric acid treatment, we can clearly observe a high current density in the SiC electrodes (Fig. 2*C*). This result indicated that no oxide layer formed on SiC, emphasizing the stability of the electronic property in SiC for faradic interfaces under high oxidation conditions, including biofluid environments. Based on an optical thin-film measurement (i.e., Nanometrics NanoSpec 210), we observed an oxide layer with an approximate thickness of 590 nm grown only on the Si area. To further estimate the amount of the consumed Si layer, we employed a depth profile scan (i.e., Dektak 150) to measure the changes in step heights of the deposited films (Fig. 2*D*). The thickness of the consumed Si layer was calculated as $t_{Si} = t_{SiO_2} - (t_{before} + t_{after})$, and it was found to be 240 nm (*SI Appendix*, Note S3 and Fig. S3). Accordingly, the ratio between the thickness of the consumed Si layer (240 nm) and that of the as-grown thermal oxide (580 nm) is 0.43:1 (i.e., 240/580 nm), consistent with Deal and Grove's oxidation model for the crystalline Si in the (100) orientation (i.e., 0.44:1) (35). The as-grown thermal oxide layer exhibits excellent uniformity over a full-scale 4-inch wafer, with a small thickness variation of less than 1% (Fig. 2*E*). The chemical inertness of SiC electrodes, along with high-quality and uniform thermal oxide layers, enables the formation of a hybrid nanomembrane structure in which SiC functions as a robust faradic interface and SiO_2 acts as a stable biobarrier for long-term flexible, implanted electronics. It is noteworthy that compared with other wide bandgap materials (e.g., bulk 4H-SiC, 6H-SiC, gallium nitride, and diamondlike carbon), our 3C-SiC-on-Si platform exhibits excellent compatibility with complementary metal-oxide semiconductor (CMOS) technology. These advantages include the applicability of rapid plasma-etching step (developed

based on Si fabrication technologies), wafer-scale–level fabrication, in situ doping techniques, and a feasible thermal oxidation approach similar to local oxidation of the Si process.

Long-Term Stability of Integrated SiC/SiO_2 Material System. Fig. 3 *A*–*C* presents optical photographs of SiC/SiO_2 electronics on Si and polyimide substrates. After transferring SiC/SiO_2 from the original Si substrate onto a flexible substrate (i.e., polyimide), our material system can be wrapped around the curvilinear surface of a glass cylinder (Fig. 3*C*). Fig. 3*D* illustrates the cross-sectional layered structure of the SiC/SiO_2 flexible electronic system, including the SiC electrodes and sensors, metal interconnects passivated by the SiO_2 thin film, and the polyimide substrate (10 μm) formed by spin coating.

Implanted devices typically experience continuous bending and folding due to either contraction or expansion of biological tissue. To investigate the mechanical flexibility of SiC/SiO_2/polyimide (PI), we employ a buckling test with a bending radius of 3 mm using a linear motor (Zaber X-LHM-E) (Fig. 3*E*). The bending curvature was chosen due to the approximate size of the sciatic nerve on the test animal. This value will be also highly applicable for the larger human nerve, which has a lower bendability requirement. The corresponding induced strain on SiC/SiO_2 was estimated to be 0.17% ($\varepsilon = 2t/R$, where t is the total thickness and R is the bending curvature), which is well within the tensile strain limits of SiC and SiO_2 of approx. 0.84% and 0.72%, respectively (32, 36). After 1,000 bending cycles, we did not observe any defect, crack, or delamination occurring on the devices. The current-voltage (I-V) characteristic of the tested devices was also recorded after every 100 bending cycles, showing excellent consistency and confirming the robustness of the SiC/SiO_2 biointerface and biobarrier under significant mechanical deformation (Fig. 3*F*). The stability of its electrical conductance indicated that there is no bandgap change in SiC after the bending test. This high flexibility is realized due to the low bending stiffness in the nanothin SiC/SiO_2 film stacked on a thin polyimide layer (10 μm). The thin substrate minimizes the distance of the functioning layer to the mechanical neutral axis, thereby reducing the induced strain onto SiC/SiO_2 (see the finite element analysis simulation result in *SI Appendix*, Note S4).

Apart from mechanical flexibility, the stability of the biointerface and biobarrier materials under hydrolysis reaction is another key feature for long-lived implantable bioelectronics. To verify, we soaked SiC and SiO_2 nanomembranes in an in vitro biosimulated electrolyte (i.e., phosphate-buffered saline [PBS 1X], pH 7.4) (Fig. 3*G* and *SI Appendix*, Note S5 for the experimental procedure). The hydrolysis experiment was performed at 96 °C as a

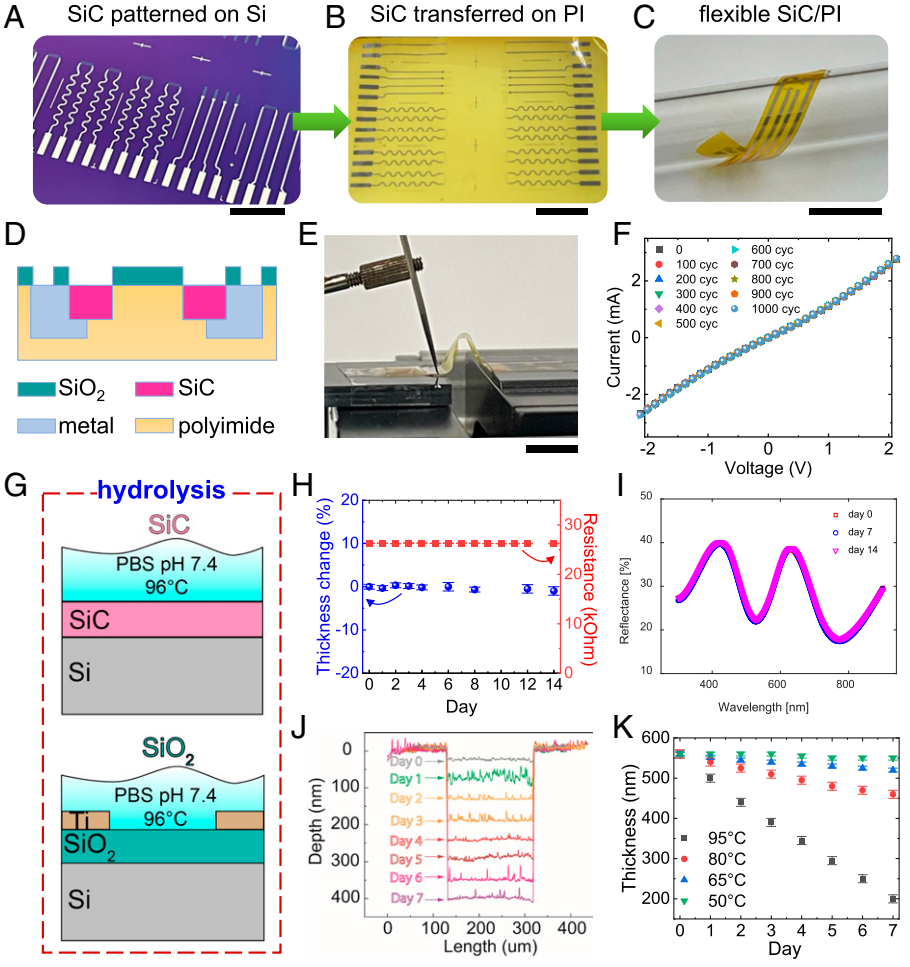

Fig. 3. Long-term stability characterizations of flexible SiC/SiO_2 electronics. (*A*) Structured SiC and metal on a Si substrate by CMOS processes. (*B*) Transferred SiC/metal onto polyimide substrate. (*C*) Bendability when wrapped around a glass tube (scale bar, 10 mm). (*D*) Cross-sectional view of flexible SiC electronics after SiO_2 passivation and metallization. (*E*) Electrical conductivity measurement of SiC during the buckling test (scale bar, 10 mm). (*F*) I-V characteristics of SiC after 1,000 bending cycles (cyc: cycle). (*G*) Soaking test of hydrolysis in SiC and as-grown SiO_2 in PBS 1X at various temperatures up to 96 °C. (*H*) SiC thickness and electrical resistance variations after the accelerated hydrolysis test in PBS at 96 °C after up to 14 days. (*I*) Optical reflectance of SiC after soaking in PBS 1X at 96 °C for 7 and 14 days. (*J*) Depth profile scan of SiO_2 in PBS 1X at 96 °C for up to 7 days. (*K*) Thickness changes of SiO_2 in PBS 1X at 96, 80, 65, and 50 °C for up to 7 days.

means of accelerating the chemical reaction, in which the lifetime of our material system can be estimated using the Arrhenius extrapolation $lifetime \propto exp(E_a/K_BT)$, where E_a is the activation energy (i.e., 1.32 eV for the case of SiO_2), K_B is the Boltzmann constant, and T is the accelerated test temperature (37). To measure the change in the thickness of SiC and SiO_2 nanomembranes, we sputtered and patterned titanium (Ti) windows with a thickness of 100 nm onto these films. As Ti rarely reacts with water molecules even at elevated temperatures, it functions as the hydrolysis mask for the subsequent depth profile measurement. Fig. 3*H* plots the thickness and electrical resistance of the SiC films against the testing period (in PBS at 96 °C). These two parameters remained almost unchanged over 14 days at 96 °C, indicating the superior stability of SiC in the biofluid environment. The stable optical property (i.e., optical reflectance) in the SiC/SiO_2 bilayer after being soaked in the PBS solution for up to 14 days suggests the suitability of SiC nanomembranes for implanted optoelectronic applications (Fig. 3*I*). Compared with SiC, SiO_2 experiences a considerably higher hydrolysis rate, which can be clearly recognized from the depth measurement (Fig. 3*J*). At 96 °C, the SiO_2 thickness reduced at a rate of approx. 50 nm/day. At lower temperatures of 80, 65, and 50 °C, the hydrolysis rate was found to be 11.5, 2.1, and 0.4 mm/day, respectively (Fig. 3*K*). By fitting the hydrolysis rate and testing temperature using the Arrhenius approximation, the lifetime of 580-nm SiO_2 at a physiological body temperature (37 °C) is estimated to be over 30 y. These results suggest that the SiC/SiO_2 material system can last for several decades, making it highly suitable for long-term implanted biomedical devices. More importantly, as the SiC is almost unaffected by the surrounding extracellular fluid, the lifetime of the device mainly depends on that of the SiO_2 insulation layer, which can be extended by increasing the film thickness. Another promising possibility is a partly biodegradable implanted system, where the dissolution timeframe is defined by the SiO_2 layers, while a minimal amount of biocompatible SiC materials would potentially be allowed to remain inside the human body.

Multimodal Electronics for Biointerfacing and Sensing. Fig. 4*A* shows an optical image of SiC bioelectrode arrays after patterning SiC, thermal oxidation of Si, and wet etching of metal interconnects. The electrochemical impedance spectra (EISs) of SiC as an active electrode were characterized in PBS 1X (pH 7.4) for a frequency ranging from 10 Hz to 1 MHz (Fig. 4*B*), using a CH Instruments CHI 660E electrochemical analyzer. At a low frequency of 10 Hz, the SiC electrodes show a relatively high impedance of ~80 kΩ. However, the impedance significantly decreased at higher frequencies and then stabilized

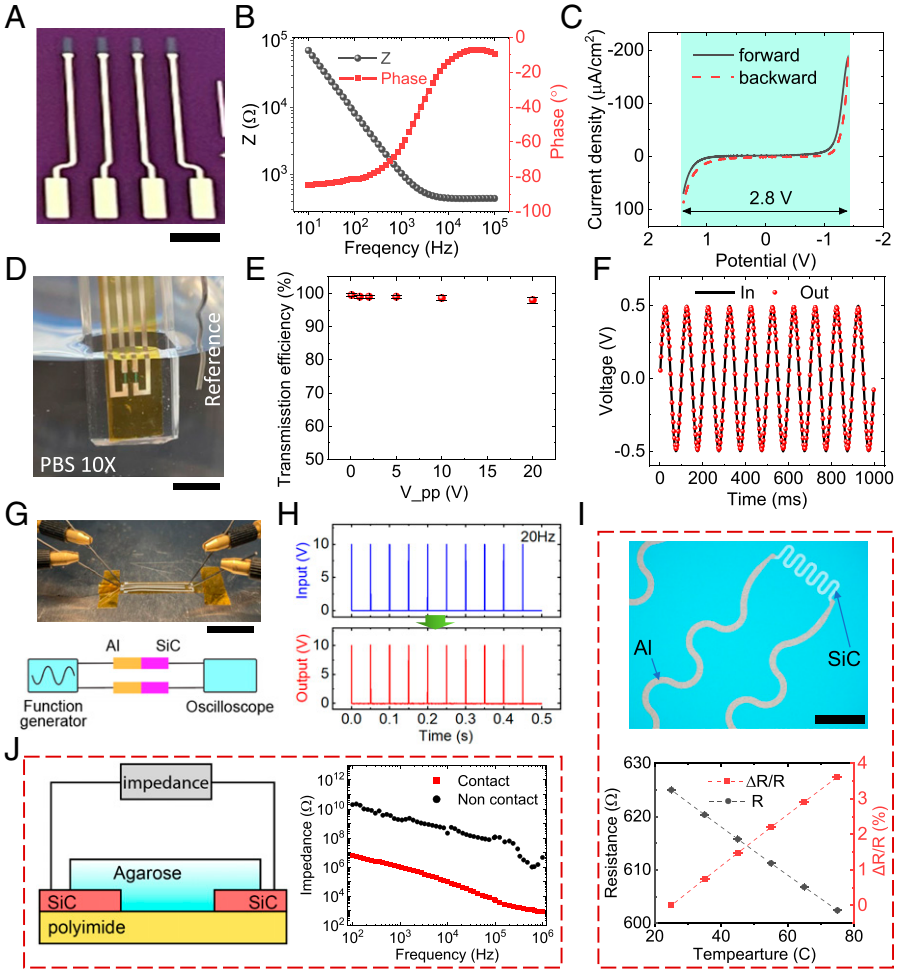

Fig. 4. Multimodal SiC/SiO_2 bioelectrodes and integrated sensors. (*A*) Optical photograph of fabricated SiC electrodes incorporated with metal contact (scale bar, 1 mm). (*B*) EIS of single-crystal SiC electrodes: impedance and phase angle versus frequency from 100 Hz to 1 MHz and electrode size of 900 × 200 μm^2 (Z: impedance). (*C*) CV scan of an SiC electrode in 0.1 M PBS (pH 7.4) at a scan rate of 0.1 V s^{-1}. (*D*) Biosimulated measurement with a Pt reference electrode in 0.1 M PBS (scale bar, 5 mm). (*E*) Transmission efficiency of alternating current (ac) electrical stimulation (V_pp: peak-to-peak voltage). (*F*) Matching output voltage with an applied ac signal at 20 Hz. (*G* and *H*) Stimulated monophasic experiment. (*G*) Experimental apparatus (scale bar, 10 mm). (*H*) Comparison between input and output signals. (*I*) Demonstration of an integrated temperature sensor (scale bar, 500 μm). (*J*) Contact sensing with a hydrogel model using SiC electrodes.

at frequencies above 6 kHz. The interfacial impedance of the SiC electrode at 1 kHz was ~1 kΩ, well within the typical range of less than 600 kΩ, which is viable for physiological applications (12). The experimental data indicate highly doped SiC is an excellent material for faradic interfaces since a lower impedance implies higher charge transfer capability. Additionally, we characterized the potential window of the active SiC electrode as a critical factor for neurological stimulation applications. Fig. 4*C* shows a cyclic voltammetry (CV) measurement of SiC electrodes in 1X PBS. Accordingly, the SiC electrode exhibited a wide potential window of −1.4 to 1.4 V, without any redox peak in the given voltage range. The potential window of 2.8 V in our n-doped 3C-SiC is one of the highest reported values, which is considerably larger than that of boron-doped diamond with an sp^2 impurity (−0.8 to 1.5 V). A wide electrochemical window can yield major advantages, including 1) safety implications for neuron stimulation with the prevention of electrochemical reactions of water and 2) the capability of detection of analytes across a wide range of electrical potentials without the interference of the background current caused by the reduction/oxidation of water. Subsequently, we calculated the charge storage capacity (CSC) as $CSC = \int_{E_C}^{E_a} i\,dE/\upsilon A$, where i (in amperes), E (in volts), υ (in volts per second), and A (in square centimeters) are the output current, applied voltage, scanning rate, and active area of the SiC electrodes, respectively (38); accordingly the CSC of the SiC electrode was found to be 735 $\mu C.cm^{-2}$ (for an opening area of 1,500 × 2,000 μm^2). This value is considerably higher than that of other common wide bandgap semiconductors (e.g., boron-doped diamond), indicating the applicability of SiC for implanted neuron stimulation (39).

Besides the characterization of SiC electrode electrochemistry, we also demonstrated the recording and stimulation function of the SiC electrode in a biosimulated environment, as shown in Fig. 4 *D*–*F*. Here, a sinusoidal signal was generated from a Pt working electrode at different magnitudes ranging from 0.1 to 20 V and at a frequency of 10 Hz (Fig. 4*D*). The emitted electrical potential propagated through the biofluid media (i.e., 1X PBS) and was captured by a flexible SiC electrode placed adjacent to the Pt electrode (Fig. 4*E*). The output voltage recorded by an oscilloscope (i.e., Keysight MSOX2022A) shows excellent gain (i.e., V_{out}/V_{in}) of ~0.98, close to the ideal value of 1 (Fig. 4*F*). We further evaluate the capability of SiC for the faradic interface using the in vitro model illustrated in Fig. 4*G*, in which stimulated monophasic signals (i.e., 10-V amplitude, 20-Hz frequency, and 1% duty cycle) were generated from a function generator. The output signal was then simultaneously picked up at the flexible SiC terminals, where it exhibits a comparable voltage (i.e., 10 V) and an identical waveform to the emitted input (Fig. 4*H*). This closely matched value between input and output signals is attributed to the electrical continuity of the metal traces, along with the low electrical resistance of the highly doped SiC nanomembranes (40). Furthermore, the EIS of the SiC stimulation electrode before and after 1 million pulse cycles was found to be almost consistent across the frequency range from 10 Hz to 100 kHz (*SI Appendix*, Fig. S9). These in vitro test results suggest a promising possibility of using SiC/SiO_2 bioelectronics to underpin in vivo biological investigations (e.g., on animal models).

Apart from being a functional faradic interface, SiC/SiO_2 electrodes can be also utilized as a multifunctional platform for real-time monitoring of multivariable biophysical parameters, providing a powerful tool for biomedical implanted applications. One of those useful functions is tissue temperature sensing, utilizing the thermoresistive effect in SiC nanomembranes. Fig. 4*I* plots the response of the SiC temperature sensors in a range from 25 to 80 °C. The significant change in the resistance with varying temperatures ($\Delta R/R \sim -3.6\%$ for $\Delta T = 50$ °C) indicates its suitability for the development of integrated thermal sensors. It should be noted that the variation in the resistance of the metal trace due to temperature is negligible, as its resistance is approximately three orders of magnitude smaller than that of SiC (i.e., below 0.1% of total resistance). The significant negative temperature coefficient of resistance ($TCR = -720$ ppm/°C) in the n-type SiC originated from the dominance of thermally activated carrier density over the decrease in electron mobility caused by phonon scattering.

Moreover, understanding the conformal contact between bioimplanted electronics and targeted tissues is critical for physiological recording and stimulation, apart from biomedical treatments such as radiofrequency ablation. The SiC impedance-sensing platform is demonstrated to effectively recognize the physical contact between electronics and biotissue. The working principle of the SiC touch sensor is based on the impedance change of the SiC electrodes under the faradic contact with tissue. Specifically, when a pair of SiC electrodes is in contact with biotissue, an additional conducting path is formed in between, which generally reduces the impedance due to the presence of conductive charges in biomaterials. We demonstrate this function using a phantom tissue made from an ionic hydrogel, a mixture of 2 wt % agarose gel and 98 wt % 0.1 M PBS (*SI Appendix*, Note S6). The contact sensor monitors the electrical impedance between two adjacent SiC electrodes (Fig. 4 *J*, *Left*). As such, when the phantom tissue was not in contact with the SiC sensor, the impedance was dominated by the oxide capacitance between the two SiC electrodes; hence, the measured impedance was in a high range (i.e., above 1 MΩ, as measured by an impedance (LCR) meter HP 4284A). When the phantom tissue creates conformal contact with the sensor, additional electrical conduction paths are formed (i.e., SiC/tissue/SiC), significantly reducing the interfacial impedance (Fig. 4 *J*, *Right*). In a frequency range of 100 Hz to 1 MHz, we observed a clear change in the impedance of SiC sensors when forming contact with phantom tissue, demonstrating the capability of the SiC electrodes for touch sensing.

Neural Stimulation on an Animal Model. The mechanical and electrochemical analyses suggested flexible SiC/SiO_2 electronics as a highly suitable platform for bioimplanted stimulation. Prior to implanting the electrodes into an animal model, we investigated the biocompatibility of the functioning material (i.e., SiC) using an in vitro cell culture approach. Particularly, the excellent optical transparency of SiC nanomembranes allows for the direct observation of cell growth and proliferation using a standard inverted microscope (see *Methods*). Fig. 5 *A*–*C* show the cell proliferation on SiC electrodes using a fluorescent imaging technique (*SI Appendix*, Note S7). Evidently, the cell counts on the SiC nanomembrane were comparable to that of the controlled sample after 5 days of growth, while cellular morphology showed that the cells are well attached onto the SiC surface (*SI Appendix*, Note S7 and Figs. S6 and S7). These results demonstrated the good biocompatibility of our material system.

In vivo nerve stimulations were carried out on an animal model (i.e., rat) to demonstrate practical biomedical applications of the soft SiC electronics for neuronal stimulation (Fig. 5*D*). After exposing the right sciatic nerve located within the gluteal region of the anesthetized rat (see *Methods* and *SI Appendix*, Note S8), the SiC electrodes were wrapped around the exposed

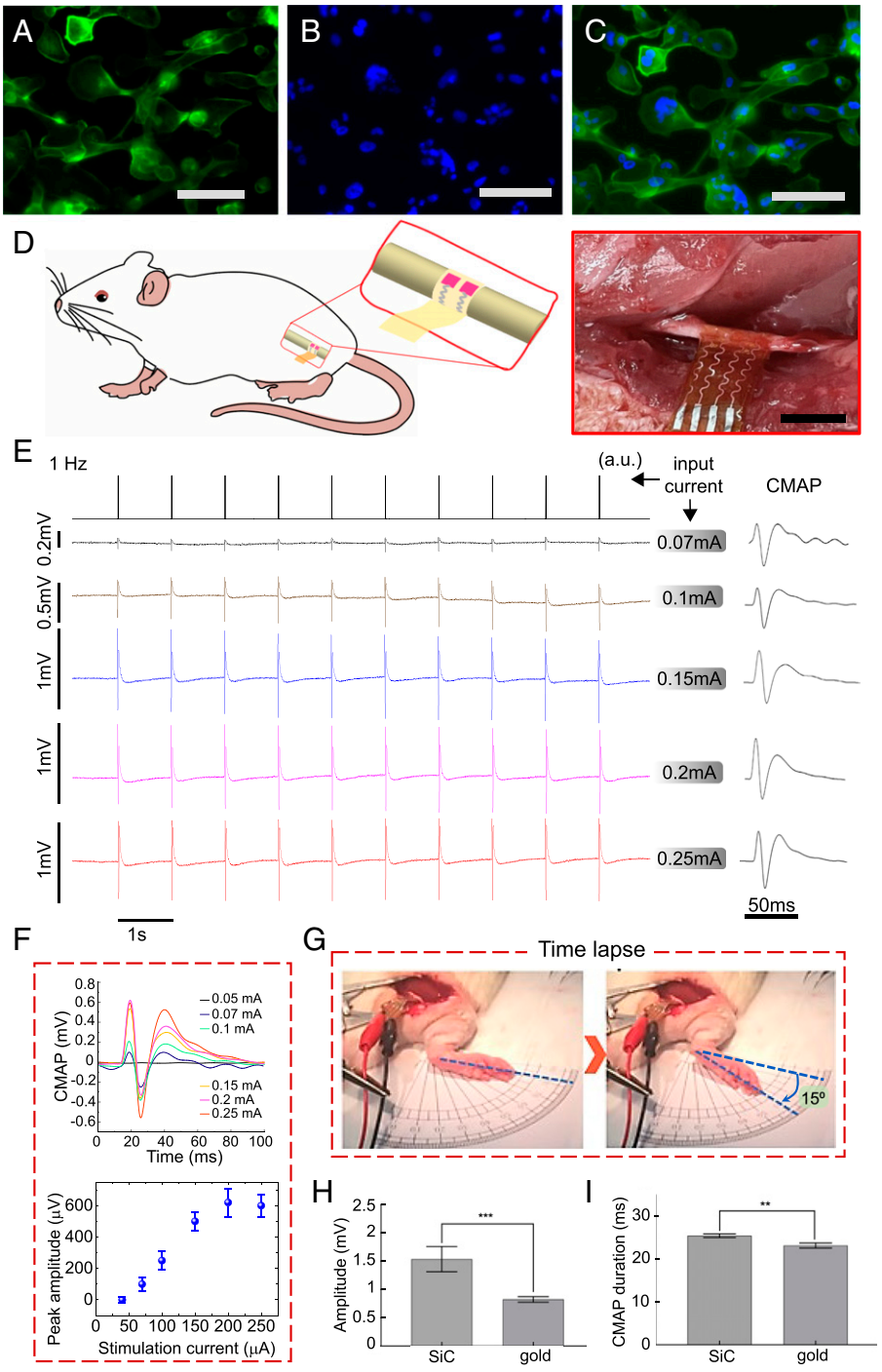

Fig. 5. (*A–C*) Biocompatibility experiment. The SiC material did not elicit cytotoxicity in the HMF. Fluorescence images: (*A*) Actin stained in green. (*B*) Nucleus stained in blue. (*C*) Merged cells: actin (green) and nucleus (blue) shows the cell attachment and spreading with their general morphology (scale bar, 50 μm). (*D–I*) Demonstration of in vivo muscle stimulation using an implanted SiC electrode. (*D*) *Left*: Schema of electrical muscle stimulation on a rat sciatic nerve model. *Right*: Photograph of flexible SiC/SiO_2 wrapped around the rat sciatic nerve (scale bar, 5 mm). (*E*) *Left*: Recorded CMAP signal from a transcutaneous surface electrode with different applied stimulating currents from 0.07 to 0.25 mA using the SiC electrode. *Right*: CMAP output waveforms (not to scale) (a.u.: arbitrary unit). (*F*) Recorded voltage amplitude at different applied pulse currents to SiC stimulation electrodes. *Up*: Overlaying the CMAP response under different stimuli. *Down*: Relationship between input current and output CMAP. (*G*) Leg movement at the knee joint with an angle of >15°. (*H* and *I*) Benchmarking stimulation of SiC versus standard gold electrodes. (*H*) Amplitude at CMAP supramaximal stimulation (mean ± standard error mean (SEM)) with significance values (***$P < 0.001$, one-tailed t-test) and (*I*) CMAP duration at supramaximal stimulation (mean ± SEM) and significance values (**$P < 0.01$, one-tailed t-test) using SiC stimulation electrodes.

sciatic nerve. Transcutaneous ring electrodes were secured around the right leg to record the compound motor action potential (CMAP) response from the gastrocnemius muscle. To verify the stimulation effectiveness of the SiC electrode, we compared the CMAP results with those of a commercial bipolar gold electrode (sourced from ADInstruments) as a control stimulator throughout the in vivo experiment (*SI Appendix*, Fig. S8). The characteristics of the stimulation impulses used for both the SiC and control groups were delivered at a 1-ms pulse width, with 10 pulses for each applied cycle at a frequency of 1 Hz. The stimulation current varied between 0.07 to 0.25 mA to assess the response from the muscle by analyzing the peak amplitude and CMAP duration. At stimulus currents below a response threshold (e.g., 0.07 mA), we did not observe any discernable

CMAP response in either group. Increasing the current intensity resulted in an onset CMAP response (Fig. 5*E*) that increased in amplitude relatively consistently and comparably with the control electrode. At stimulus currents above 0.2 mA, the recorded CMAP response reached its supramaximal response and remained constant even when increasing the current intensity. This observation is reasonable as the evoked supramaximal CMAP response is typically the summation of the action potentials generated from all the activated motor axons within the whole sciatic nerve. A low current intensity (<0.07 mA) may only excite a small number of axons, which is not recordable with the surface electrodes. Increasing the stimulus current leads to a rise in the number of activated motor axons, resulting in a higher compounded voltage in the innervated muscle (e.g., gastrocnemius). When the stimulus current reached ∼0.2 mA (for both the SiC electrode and control), most motor axons were assumed to be activated due to the CMAP amplitude reaching its supramaximal signal (Fig. 5*F*). Sufficient stimulus current can be visually observed that generates leg movement at the knee joint angle, resulting in ∼15° of displacement (Fig. 5*G*). The movement of the leg under electrical stimulation suggests a promising possibility of using flexible, implanted SiC/SiO_2 electronics to regain limb control in patients with paralysis. It should be noted that at a higher stimulus current, which resulted in the leg movement, the SiC/SiO_2 nanomembranes maintained good conformal contact with the sciatic nerve, which is reflected by the stable and constant CMAP signal over 10 continuous pulses. The CMAP amplitude and duration at a supramaximal response generated from the SiC electrodes and the control device were extracted from the action potential recording and plotted in Fig. 5 *H* and *I*. CMAP amplitude is a neurophysiological parameter that represents the number of motor axons active during stimulation (41). In these series of experiments, the SiC electrode displayed a mean amplitude of 1.54 ± 0.22 mV ($n = 3$), while the control (gold electrode) displayed a mean amplitude of 0.82 ± 0.05 mV ($n = 3$). The SiC electrode displayed a significantly higher ($P = 0.0008$) amplitude than the control. This difference could be explained by the greater conformal surface area contact between the interface of the SiC electrode and epineurium of the sciatic nerve, resulting in a greater number of active motor axons and thus supplying more muscle fibers and increasing the CMAP amplitude.

The CMAP duration in neurophysiological studies represents the synchrony of firing of the motor neurons and thus coordinated active muscle contraction (42, 43). Our results display a significant difference in duration (in milliseconds) between the SiC electrode and the control ($P = 0.0016$; $n = 3$). The mean duration of the control was 23.21 ± 0.60 ms, and that of the SiC electrode was 25.49 ± 0.45 ms. The difference seen between the two electrodes could be explained simply by the fact that if fewer axons were activated (as mentioned above) due to the interface contact of the control electrode to the epineurium, then fewer muscle fibers are required to fire in synchrony. Another plausible explanation for this increase in CMAP duration is the distance between the anode and the cathode of the stimulating electrode, which was considerably shorter in the control compared with the SiC, which wrapped around the entire nerve's circumference. However, it must be acknowledged that one of the pitfalls of nerve-conduction studies is the movement of the recording electrodes during supramaximal stimulation. This is somewhat unavoidable, particularly when changing between different stimulating electrodes and when there is significant limb movement of the animal's lower extremity. Nonetheless, it is evident that the SiC electrodes can successfully stimulate the peripheral nerve comparable to a standard gold control, as shown in *SI Appendix*, Fig. S8.

Conclusion

The present work introduces an innovative material platform and proof of concept for long-lived implanted electronics, using highly doped SiC as functional faradic interfaces and a thermally grown oxide layer as a robust biobarrier. The self-passivation process for SiC bioelectronics facilitates the direct contact of SiC electrodes with targeted tissues. Experimental results suggest the extremely low hydrolysis in SiC/SiO_2 hybrid structures can enable underlying electronic components to last for several decades and potentially over the lifetime of patients with long-lived functions. The characterizations of the mechanical flexibility and electrical stability under a cyclic bending test of flexible SiC/SiO_2 on polyimide indicated the ability of conformal contact formations with biotissue. Furthermore, in vivo studies on an animal model validated the feasibility and capability of flexible SiC electrodes for neuron stimulation, which can be clearly observed through the muscle action potentials. From the manufacturing perspective, the compatibility with the CMOS process of the SiC-on-Si platform offers reproducibility and scalable fabrication. In addition, our growth process employing carbonization of Si to form SiC thin films suggests the possibility of depositing the material on silicon-on-insulator (SOI) wafers. An ideal SiC-on-insulator platform could allow for different fabrication routes for flexible devices where SiC functions as the electronics interface, while the box oxide layer provides electrical insulation. However, as the current CVD temperature is relatively high (i.e., 1,250 °C), reducing the growth temperature to ensure the dielectric properties of the oxide is imperative to integrate other functional components, such as Si-based thin-film transistors under the SiC/SiO_2 biobarrier. This development would expand the capability of the present implantable SiC electronic platform for central and peripheral neurological mapping and modulations.

Methods

SiC Material Development. Atomic SiC layers were deposited onto a Si substrate using a hot-wall chamber (i.e., Epiflex) at a temperature of 1,250 °C. To remove native oxide and organic residuals, the Si substrate was thoroughly cleaned using a standard cleaning procedure (i.e., Radio Corporation of America cleaning). The Si surface was first carbonized to facilitate alternating supply of epitaxy cycles of silane and ethane gases to provide Si and carbon precursors. *N*-type doped SiC was formed using an in situ doping method using NH_3.

SiO_2 Passivation. The wet oxidation process of the SiC-on-Si wafer was performed in a semiconductor-type diffusion furnace (i.e., HiTech Furnaces UK). Oxidation was sourced from water vapor at 96 °C with a carrier gas (i.e., nitrogen). Water vapor pressure and temperature were precisely controlled throughout wet oxidation at a temperature of 900 ± 0.5 °C for 10 h.

Device Fabrication. From an as-grown SiC-on-Si wafer, the SiC layer was patterned to obtain SiC structures on the Si substrate. After the SiC-on-Si wafer was oxidized, the backside oxide layer was removed by a standard oxide removal procedure. The front side with the patterned SiC was deposited with a metal layer and then wet etched to form interconnects. Flexible substrate (i.e., polyimide) was spin coated with a thickness of 10 μm to ensure flexibility. The host Si substate was completely removed by two dry-etching steps. Oxide windows were created by standard photolithography and wet oxide etching. Further details are available in *SI Appendix*, Notes S1 and S2 and Figs. S1 and S2.

Electrochemical Analysis. The electrochemical analysis on the prepared SiC membrane was conducted in a CHI 660E electrochemical analyzer (CH Instruments) using a single-compartment cell with a three-electrode configuration, with SiC as the working electrode, the Pt gauze as the counterelectrode, and a reference silver/silver chloride (Ag/AgCl) electrode. The redox peaks were

analyzed by CV under a potential window of ±1.4 V (vs. Ag/AgCl) at 100 $mV.s^{-1}$, while EISs were performed at open circuit potential (−0.5 V). Both analyses were performed under an ambient condition containing 1X PBS as the electrolyte.

Cell Culture Protocol. Human mammary fibroblasts (HMFs), sourced from ATCC, Australia, were grown and maintained in Dulbecco's modified eagle medium/nutrient mixture f-12 (DMEM/F12) (Gibco, Thermo Fisher Scientific, Waltham, MA, USA) medium with 10% fetal bovine serum and 1% penicillin/streptomycin. The cells were cultured in T75 flasks at 37 °C in a humidified atmosphere with 5% CO_2. The cells were harvested at 80% confluency. Prior to seeding the cells on the test material for the biocompatibility assay, test material (SiC) was sterilized with 80% ethanol and washed three times with sterile 1X Hank's balanced salt solution followed by ultraviolet (UV) radiation for 30 min. The cells were seeded on the sterile material and were further analyzed for cell morphology and cell proliferation assay.

In Vivo Sciatic Nerve Stimulation. All the procedures were approved by the Research Information Management System, Animal Research Ethics (protocol ENG/01/21/AEC). Three adult male Wistar rats aged 3 mo, with an average weight 450 g, were used for the experiment. Surgery was performed on the right sciatic nerve. The sensing surface ring electrode (red) was positioned where the gastrocnemius muscle has its maximum diameter. The reference surface ring electrode (black) was placed just beneath the sensing electrode. Contact gel was employed to optimize the conductivity/transfer resistance. A skin incision was performed extending from a midpoint (between the hip joint and ischial tuberosity) to the knee. Blunt dissection was carried out (muscle splitting approach) using Iris scissors between the gluteus maximus and biceps femoris muscle. The sciatic nerve was identified under the gluteus maximus muscles. The nerve was isolated from the surrounding connective tissues and fascia using microscissors. The epineurium and its blood vessels were preserved. Gold was selected as the control electrode as it is a noble metal with good biocompatibility, high conductivity, and low impedance. For an extracellular nerve recording and/or stimulation, where invariably the animal will be euthanized as an endpoint of the experiment, due to the invasiveness of the procedure (not the material), the gold-stimulating electrode would be appropriate.

Data Availability. All study data are included in the article and/or *SI Appendix*.

ACKNOWLEDGMENTS. This work was partially funded by Discovery Grant DE200100238 from the Australian Research Council, the Griffith University Integrated Microelectronic Platform for Advanced Health-Care Spotlight, and UNSW GROW Early Career Academics Grant (PS66725). T.-K.N. acknowledges support from a Griffith University postdoctoral fellowship. Y.Y. acknowledges support from Japan Science and Technology Agency - Exploratory Research for Advanced Technology (JST-ERATO) (Yamauchi Materials Space-Tectonics Project, Grant JPMJER2003), Japan. This work was performed in part at the Queensland node of the Australian National Fabrication Facility, a company established under the National Collaborative Research Infrastructure Strategy to provide nano- and microfabrication facilities for Australia's researchers. This publication was supported by the UNSW Faculty of Engineering Open-Access Publishing Award. The authors would like to thank Prof. John A. Rogers at Northwestern University for his valuable discussion on long-lived flexible electronics.

Author affiliations: [a]Queensland Micro and Nanotechnology Centre, Griffith University, Brisbane, Queensland 4111, Australia; [b]School of Nursing and Midwifery, Griffith University, Gold Coast, Queensland 4215, Australia; [c]Australian Institute for Bioengineering and Nanotechnology, The University of Queensland, Brisbane, Queensland 4072, Australia; [d]Sensing System Research Center, The National Institute of Advanced Industrial Science and Technology, Tsukuba, Ibaraki 305-8560, Japan; [e]Centre for Future Materials, University of Southern Queensland, Springfield Central, Queensland 4305, Australia; [f]JST-ERATO Yamauchi Materials Space-Tectonics Project, National Institute for Materials Science (NIMS), Tsukuba, Ibaraki 305-0044, Japan; [g]International Center for Materials Nanoarchitectonics (WPI-MANA), National Institute for Materials Science (NIMS), Tsukuba, Ibaraki 305-0044, Japan; and [h]School of Mechanical and Manufacturing Engineering, The University of New South Wales, Sydney, New South Wales 2052, Australia

Author contributions: T.-K.N. and H.-P.P. designed research; T.-K.N., M.B., A.A., T.-A.T., S.Y., M.L., L.H., and H.-P.P. performed research; M.B., Y.Y., and H.-P.P. contributed new reagents/analytic tools; T.-K.N., M.B., A.A., T.-A.T., S.Y., M.L., T.-V.N., N.K., T.D., Y.Y., N.-T.N., and H.-P.P. analyzed data; and T.-K.N., M.B., A.A., T.D., Y.Y., N.-T.N., and H.-P.P. wrote the paper.

1. F. B. Wagner *et al.*, Targeted neurotechnology restores walking in humans with spinal cord injury. *Nature* **563**, 65–71 (2018).
2. I. Peña Pino *et al.*, Long-term spinal cord stimulation after chronic complete spinal cord injury enables volitional movement in the absence of stimulation. *Front. Syst. Neurosci.* **14**, 35 (2020).
3. A. L. Behrman, E. M. Ardolino, S. J. Harkema, Activity-based therapy: From basic science to clinical application for recovery after spinal cord injury. *J. Neurol. Phys. Ther.* **41** (suppl. 3), S39–S45 (2017).
4. M. L. Jones *et al.*, Activity-based therapy for recovery of walking in individuals with chronic spinal cord injury: Results from a randomized clinical trial. *Arch. Phys. Med. Rehabil.* **95**, 2239–46.e2 (2014).
5. T. Someya, Z. Bao, G. G. Malliaras, The rise of plastic bioelectronics. *Nature* **540**, 379–385 (2016).
6. M. Y. Rotenberg, B. Tian, Bioelectronic devices: Long-lived recordings. *Nat. Biomed. Eng.* **1**, 0048 (2017).
7. S. W. Kemp, P. S. Cederna, R. Midha, Comparative outcome measures in peripheral regeneration studies. *Exp. Neurol.* **287**, 348–357 (2017).
8. J. Koo *et al.*, Wireless bioresorbable electronic system enables sustained nonpharmacological neuroregenerative therapy. *Nat. Med.* **24**, 1830–1836 (2018).
9. L. Ulloa, The vagus nerve and the nicotinic anti-inflammatory pathway. *Nat. Rev. Drug Discov.* **4**, 673–684 (2005).
10. Z. Xiang *et al.*, Progress of flexible electronics in neural interfacing–A self-adaptive non-invasive neural ribbon electrode for small nerves recording. *Adv. Mater.* **28**, 4472–4479 (2016).
11. E. Song *et al.*, Flexible electronic/optoelectronic microsystems with scalable designs for chronic biointegration. *Proc. Natl. Acad. Sci. U.S.A.* **116**, 15398–15406 (2019).
12. E. Song, J. Li, S. M. Won, W. Bai, J. A. Rogers, Materials for flexible bioelectronic systems as chronic neural interfaces. *Nat. Mater.* **19**, 590–603 (2020).
13. X. Li *et al.*, Pulsation of electrified jet in capillary microfluidics. *Sci. Rep.* **7**, 5673 (2017).
14. A. Jonsson *et al.*, Therapy using implanted organic bioelectronics. *Sci. Adv.* **1**, e1500039 (2015).
15. J. H. Koo, J.-K. Song, D.-H. Kim, D. Son, Soft implantable bioelectronics. *ACS Mater. Lett.* **3**, 1528–1540 (2021).
16. R. A. Normann, Technology insight: Future neuroprosthetic therapies for disorders of the nervous system. *Nat. Clin. Pract. Neurol.* **3**, 444–452 (2007).
17. Y. Zhang *et al.*, Climbing-inspired twining electrodes using shape memory for peripheral nerve stimulation and recording. *Sci. Adv.* **5**, eaaw1066 (2019).
18. H. Wu, W. Gao, Z. Yin, Materials, devices and systems of soft bioelectronics for precision therapy. *Adv. Healthc. Mater.* **6**, 1700017 (2017).
19. S. K. Kang *et al.*, Bioresorbable silicon electronic sensors for the brain. *Nature* **530**, 71–76 (2016).
20. T. A. Truong *et al.*, Engineering stress in thin films: An innovative pathway toward 3D micro and nanosystems. *Small* **18**, e2105748 (2022).
21. Y. S. Choi *et al.*, Stretchable, dynamic covalent polymers for soft, long-lived bioresorbable electronic stimulators designed to facilitate neuromuscular regeneration. *Nat. Commun.* **11**, 5990 (2020).
22. Y. Li, N. Li, N. De Oliveira, S. Wang, Implantable bioelectronics toward long-term stability and sustainability. *Matter* **4**, 1125–1141 (2021).
23. I. R. Minev *et al.*, Biomaterials. Electronic dura mater for long-term multimodal neural interfaces. *Science* **347**, 159–163 (2015).
24. W. Yan *et al.*, Structured nanoscale metallic glass fibres with extreme aspect ratios. *Nat. Nanotechnol.* **15**, 875–882 (2020).
25. C. H. Chiang *et al.*, Development of a neural interface for high-definition, long-term recording in rodents and nonhuman primates. *Sci. Transl. Med.* **12**, eaay4682 (2020).
26. H. Fang *et al.*, Capacitively coupled arrays of multiplexed flexible silicon transistors for long-term cardiac electrophysiology. *Nat. Biomed. Eng.* **1**, 0038 (2017).
27. J. Li *et al.*, Ultrathin, transferred layers of metal silicide as faradaic electrical interfaces and biofluid barriers for flexible bioelectronic implants. *ACS Nano* **13**, 660–670 (2019).
28. T. A. Pham *et al.*, A versatile sacrificial layer for transfer printing of wide bandgap materials for implantable and stretchable bioelectronics. *Adv. Funct. Mater.* **30**, 2004655 (2020).
29. J. Rozman *et al.*, Heart function influenced by selective mid-cervical left vagus nerve stimulation in a human case study. *Hypertens. Res.* **32**, 1041–1043 (2009).
30. M. P. Neuser *et al.*, Vagus nerve stimulation boosts the drive to work for rewards. *Nat. Commun.* **11**, 3555 (2020).
31. Z. Mridha *et al.*, Graded recruitment of pupil-linked neuromodulation by parametric stimulation of the vagus nerve. *Nat. Commun.* **12**, 1539 (2021).
32. T. K. Nguyen *et al.*, Superior robust ultrathin single-crystalline silicon carbide membrane as a versatile platform for biological applications. *ACS Appl. Mater. Interfaces* **9**, 41641–41647 (2017).
33. T. Nguyen *et al.*, Giant piezoresistive effect by optoelectronic coupling in a heterojunction. *Nat. Commun.* **10**, 4139 (2019).
34. H. P. Phan *et al.*, Long-lived, transferred crystalline silicon carbide nanomembranes for implantable flexible electronics. *ACS Nano* **13**, 11572–11581 (2019).
35. A. Pasquarello, M. S. Hybertsen, R. Car, Interface structure between silicon and its oxide by first-principles molecular dynamics. *Nature* **396**, 58–60 (1998).
36. W. N. Sharpe *et al.*, Strain measurements of silicon dioxide microspecimens by digital imaging processing. *Exp. Mech.* **47**, 649–658 (2007).
37. H. Fang *et al.*, Ultrathin, transferred layers of thermally grown silicon dioxide as biofluid barriers for biointegrated flexible electronic systems. *Proc. Natl. Acad. Sci. U.S.A.* **113**, 11682–11687 (2016).
38. H. S. Kim *et al.*, Oxygen vacancies enhance pseudocapacitive charge storage properties of MoO_{3-x}. *Nat. Mater.* **16**, 454–460 (2017).
39. D. J. Garrett, W. Tong, D. A. Simpson, H. Meffin, Diamond for neural interfacing: A review. *Carbon* **102**, 437–454 (2016).
40. J. Li *et al.*, Conductively coupled flexible silicon electronic systems for chronic neural electrophysiology. *Proc. Natl. Acad. Sci. U.S.A.* **115**, E9542–E9549 (2018).
41. M. A. Anderson *et al.*, Astrocyte scar formation aids central nervous system axon regeneration. *Nature* **532**, 195–200 (2016).
42. A. Mallik, A. I. Weir, Nerve conduction studies: Essentials and pitfalls in practice. *J. Neurol. Neurosurg. Psychiatry* **76** (suppl. 2), ii23–ii31 (2005).
43. S. Lee *et al.*, Selective stimulation and neural recording on peripheral nerves using flexible split ring electrodes. *Sens. Actuators B Chem.* **242**, 1165–1170 (2017).